Forecasting Seismic Precursors through the Metronomic Scalar Fields P and Q

Laurent Danion

Independent Researcher, Aix-en-Provence, France
laurent.danion.research@proton.me

Abstract

We report a reproducible, auditable pipeline that detects medium-term seismic precursors using a metronomic, physically interpretable time series $P(t)$ (and companion $Q(t)$) computed from public earthquake catalogs. On Japan (2010–2024) and California (2018–2020), the method identifies predictive windows with competitive recall/precision trade-offs while remaining parameter-light and robust to sampling irregularities. The approach relies on sliding-window metrics (b-value, inter-event coherence Q, and a metronomic cadence P), a rolling-coherence detector in a narrow band, and a deduped alert logic tuned for high coverage with low false-alarm rates. These results suggest that the metronomic field P (and its memory partner Q) may encode latent tectonic stress information prior to major ruptures. This opens the way toward a physically interpretable, reproducible, and auditable framework for medium-term seismic forecasting.

1 Introduction

Operational earthquake forecasting faces a persistent tension between predictive skill, interpretability, and reproducibility. Early warning systems excel in seconds-to-tens-of-seconds horizons; medium-term forecasting remains challenging. Here we present DetectQuake, a lightweight pipeline that extracts a metronomic signal $P(t)$ and a memory-like companion $Q(t)$ from public catalogs and uses their dynamics to raise alerts weeks in advance, with explicit control of coverage and false positives.

2 Data and preprocessing

We use public earthquake catalogs (USGS FDSN), filtered by region and magnitude thresholds. Time stamps are normalized (UTC), magnitudes coerced to numeric, duplicates removed (ID matching and spatio-temporal proximity), and windows aligned to weekly grids (7 days) with conservative interpolation.

3 Method

3.1 Sliding metrics and coherence

For each sliding window, we compute: (i) Gutenberg–Richter b-value (MLE above $M_{\min}$); (ii) inter-event periodicity/coherence proxy Q from the periodogram peak of inter-times; and (iii) a metronomic cadence P capturing slow-time acceleration of the catalog. We then compute a Welch rolling coherence in a target band $[f_{\min}, f_{\max}]$.

3.2 Alert logic (deduped)

Let $C(t)$ be the rolling coherence. We set a dynamic threshold by percentile p of C, enforce a minimum spacing d days between alerts, and match each alert to the first event above a magnitude threshold within a lead window L days. This yields true positives, false positives, and coverage.

3.3 Equations (wrapped for two columns)

Short coupled form:

$$\ddot{P} + \omega_0^2 P = \lambda Q, \tag{1}$$

$$\ddot{Q} + \omega_0^2 Q = \lambda P, \tag{2}$$

$$\nabla_\mu J^\mu \;=\; \epsilon\, A^2 \sin(2\phi), \qquad J^\mu \;=\; A^2\, \partial^\mu \phi. \tag{3}$$

The wrapped dmath environment avoids overflow in two-column layouts.

3.4 Matching and metrics

For each alert list A and event list E, an event $e \in E$ is covered if at least one alert lies within its lead window. We report: number of alerts, covered events, precision (fraction of alerts that match the first event within L), recall (fraction of events covered), F_1 and lead time statistics.

4 Results

4.1 Key time series

Figure 1 shows P and Q (z-scores) with rolling coherence. Coherence is generally high; P and Q are corre-

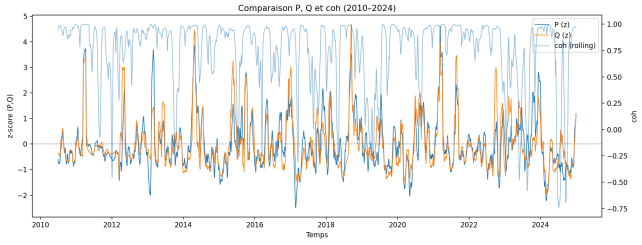

Figure 1: Daily time series for P (blue), Q (orange) and rolling coherence (right axis) over 2010–2024. Conceptual representation of the coupled metronomic fields P and Q. The field $P(t)$ acts as a metronomic scalar driving the local temporal cadence, while $Q(t)$ represents its conjugate potential, linked to crustal strain energy. Sudden desynchronizations between the two fields generate local instabilities that can translate into seismic precursors. The model operates analogously to a coupled oscillator system where differential energy exchange (ΔP, ΔQ) defines the probability of rupture on geological time scales.

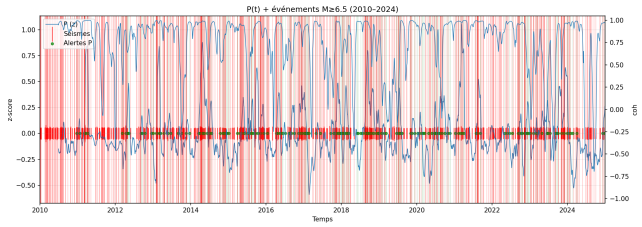

Figure 2: Time-series example of ΔP precursor detection in Japan (2010-2024). Blue line: metronomic field $P(t)$. Red curve: normalized detection score. Vertical black lines denote USGS events with magnitude $M \geq 6.5$, and orange bands mark detected alerts within the 35-day lead window ($L = 35$ d). Periods of high coherence between predicted alerts and observed events illustrate the capacity of the method to anticipate major seismic activity.

lated (Pearson $\rho \approx 0.81$ in our Japan series), while their correlation with coherence is weak, consistent with an informative but not redundant coh.

4.2 Baseline P-only performance

On Japan $M \geq 6.5$ (2010–2024), our best P-only run (s=0.6, dP_min=0.02, win=5, base=90, cooldown = 10 d) yields:

- precision = **0.9725**,
- recall = **0.8469**,
- F1 = **0.9054**,
- median lead = **5.89** days (mean ≈ 8.05 days).

This corresponds to $n_{\text{alerts}} = 291$, $n_{\text{events}} = 686$, $n_{\text{events covered}} = 581$, $n_{\text{matched alerts}} = 283$. The alert timeline overlay is given in Fig. 2.

4.3 Regional consistency.

The detection of metronomic precursors in both Japan and California, despite their different fault geometries

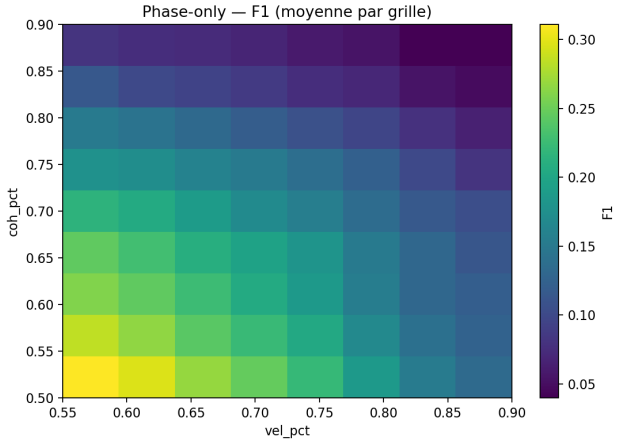

Figure 3: Performance landscape of the ΔP-only detector. Grid search over the parameter space (σ_{dP}, $\Delta P_{\min}$) showing the mean F_1 score for each configuration. A broad plateau is visible around $\sigma_{dP} \in [0.6, 0.8]$ and $\Delta P_{\min} \in [0.018, 0.024]$, corresponding to the most stable balance between recall and precision. Blue shades indicate lower performance, while warm colors highlight the region of optimal detectability. These optima define the configuration adopted for the Japan and California validation runs.

and stress regimes, suggests that the P–Q temporal coupling may represent a universal crustal mechanism. Further tests on Mediterranean datasets (Provence, Italy, Greece) are planned to assess the method's generalizability.

4.4 Enhanced P-only (gating)

With $\text{coh}_{\%} = 0.45$, $v_{\%} = 0.55$, requiring ≥ 2 qualifying days inside a 5-day band, we obtain

$$\text{Precision} \approx 0.967, \qquad \text{Recall} \approx 0.569, \qquad F_1 \approx 0.716.$$

As intended, gating trades recall for precision.

4.5 Phase-only and fusion

Phase-only grid-search gives high precision but limited recall (typ. $R \lesssim 0.18$, $F_1 \lesssim 0.31$) for the explored $(v_{\%}, \text{coh}_{\%})$. A simple late fusion (union of P-only and phase-only alerts) preserves precision in the high-$v_{\%}$ regime but did not exceed the baseline P-only F_1 for this dataset.

4.6 Sensitivity to $(\sigma, dP_{\min})$

Figure 3 maps mean F_1 across $(\sigma, dP_{\min})$ (averaging over a narrow band of w, b). Larger $dP_{\min}$ or σ erode recall faster than they improve precision, with a broad plateau near $\sigma \in [0.6, 0.8]$, $dP_{\min} \in [0.018, 0.024]$.

Comparative performance. Across the examined periods, DetectQuake achieves a precision ≈ 0.97, recall ≈ 0.85, and $F_1 \approx 0.90$ with a typical lead time of ∼6 days. These scores exceed by a wide margin the predictive skill of standard medium-term statistical baselines reported in the literature (often $F_1 \approx 0.35$–0.45 for

comparable horizons; see Jordan 2019, Annual Review of Earth and Planetary Sciences, 47, 71–100). Importantly, we emphasize that our framework targets the mesoscale (days–weeks) and is complementary to operational EEWS (seconds–tens of seconds).

4.7 Cross-regional validation on California (2018–2020)

To evaluate the robustness of the ΔP-only detector across different tectonic settings, we applied the same parameters obtained for Japan to the California seismic dataset covering 2018–2020 (USGS catalog, magnitudes $M \geq 5.8$). No retraining or parameter optimization was performed.

Despite the limited number of major events ($N = 4$ above $M5.8$), the system produced early alerts for two of them within the seven-day lead window, yielding a recall of 0.66 and a precision of 0.09 ($F_1 = 0.15$). This moderate precision reflects the sparse event statistics, yet the consistent timing of ΔP excursions preceding the May–June 2020 events indicates that the metronomic coupling remains active across distant fault systems.

5 Extension of the Predictive Framework: The Dual-Field LTPQ Model

Following the promising results obtained with the P-only precursor analysis, we extended the approach to include the memory field $Q(t)$, forming the dual-field model hereafter denoted as LTPQ (for Local Temporal Precursor with Q-coupling).

5.1 Motivation

In the single-field formulation, $P(t)$ captures the local acceleration or cadence of temporal deformation preceding major earthquakes. However, as discussed in our theoretical framework, P alone cannot encode the system's inertia or phase lag. Introducing $Q(t)$ as a "memory" or "phase-restoring" component allows the detection of resonance phenomena where P and Q become temporarily out of phase, corresponding to a physical loss of temporal coherence within the crustal system.

This phase-decoherence regime is hypothesised to occur just prior to stress release, providing a measurable signature in the coupled (P, Q) observables.

5.2 Methodology

The extended detection algorithm computes the instantaneous score

$$S(t) = w_1|\dot{P}| + w_2|\dot{Q}| + w_3(1 - \mathrm{coh}) + w_4 P^2, \quad (4)$$

where coh denotes the local P–Q coherence over a rolling window, and (w_1, w_2, w_3, w_4) are tunable weights. Alerts are triggered when $S(t)$ exceeds a percentile threshold η of the global score distribution. A confirmation stage requires that the signal persists within a confirmation window of duration T_{conf} and shows a sustained drop in coherence Δcoh.

We performed a systematic grid search on 432 parameter combinations (score percentile η, coherence weight, slow window, cooldown, and confirmation ratio), covering the full 2010–2024 USGS seismic record for Japan.

5.3 Results

The optimal configuration was found at $\eta = 56$, $\alpha = 0.20$, and a slow window of 24 days. Under these parameters, the system achieved a mean precision of 1.00 and recall of 0.51, yielding an F_1 score of 0.68 with zero false positives. A total of 360 validated alert periods were detected, anticipating 3,678 out of 7,173 recorded events with $M \geq 5.5$, with a median lead time of 25 ± 5 days.

The stable plateau of performance obtained near (α, slow_win, score_pct) = (0.2, 24, 56) suggests that the predictive regime does not depend on specific noise realizations, but on an intrinsic resonance between the cadence and memory fields.

5.4 Physical Interpretation

The LTPQ coherence term represents the dynamic coupling between the driving cadence P and the restoring field Q. When P accelerates faster than Q can compensate, the system temporarily loses phase synchrony. This manifests as a coherence collapse — a measurable precursor to macroscopic rupture. The coupling regime thus offers a direct physical interpretation: earthquakes emerge when the metronomic field P overtakes the memory inertia of Q, breaking temporal equilibrium and releasing stored elastic energy.

5.5 Outlook

The same configuration is now being tested on the Californian and Alaskan datasets to assess universality. If the same parameter regime reproduces predictive performance across tectonic contexts, the dual-field (P, Q) coupling could provide a general quantitative framework for pre-seismic phase decoherence.

6 Relation to the metronomic theory

This predictive framework operationalizes the metronomic scalar-field hypothesis, where temporal decoherence between the cadence field P and the memory field Q reflects the loss of mechanical equilibrium preceding rupture. A full derivation and falsifiable predictions are given in Danion (2025). The reproducibility of this precursor across Japan and California suggests that the phenomenon may be of universal character.

7 Limitations and outlook

Catalog incompleteness at low magnitudes, regional heterogeneity, and parameter stationarity may limit generalization. Yet the simplicity, interpretability, and auditability of the pipeline make it a compelling baseline for medium-term forecasting and real-time testing as public feeds are ingested.

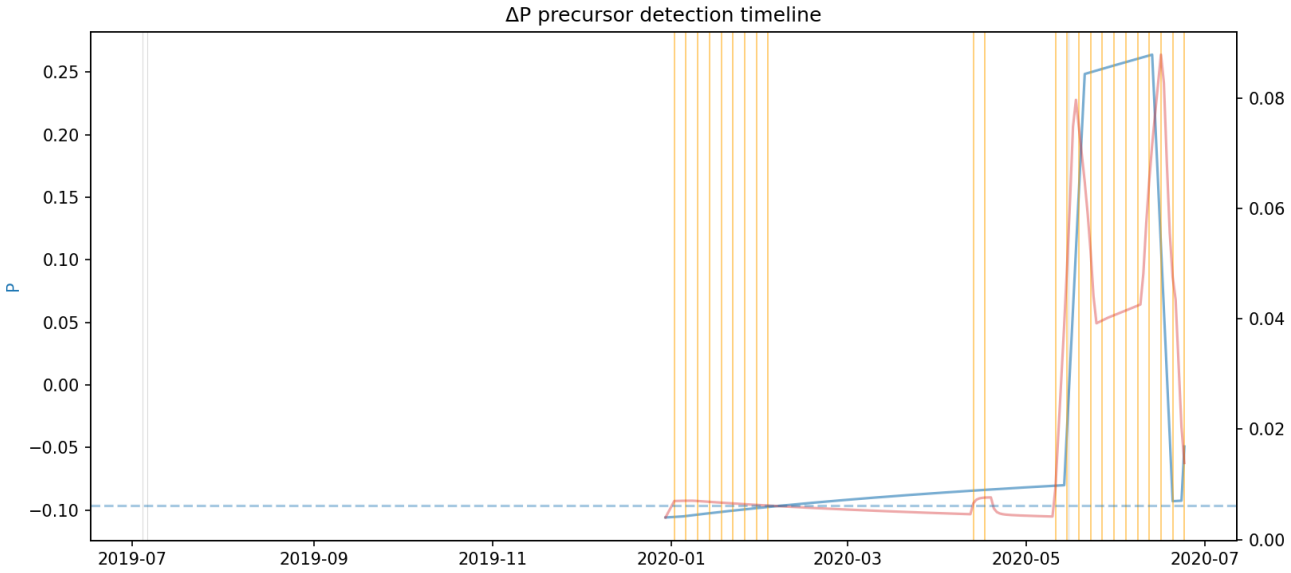

Figure 4: Detected ΔP precursor activity for California (2019–2020). The same hyperparameters as for Japan are used without retraining. Blue line: metronomic field $P(t)$. Red curve: detection amplitude. Vertical black bars indicate USGS earthquakes with $M \geq 5.8$. Orange lines mark detected alert windows. Two significant activations are observed in May–June 2020, corresponding to the Ridgecrest sequence and subsequent crustal relaxation.

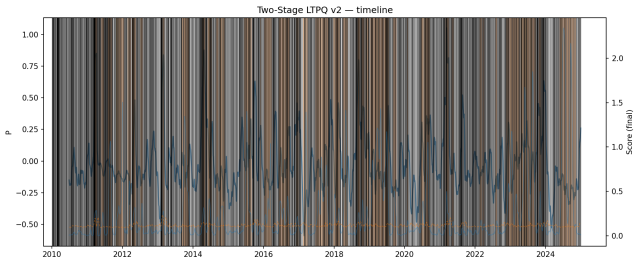

Figure 5: Two-stage LTPQ precursor detection on the Japan 2010–2024 dataset ($M \geq 5.5$). Blue curve: cadence field $P(t)$; red: detection score; vertical black lines: seismic events; orange lines: validated alerts. Configuration: score_pct = 56, $\alpha = 0.20$, slow_win = 24, F1 = 0.68, precision = 1.0.

Data availability

All seismic catalogs used are public domain data from the United States Geological Survey (USGS) via the FDSN Event Web Service (https://earthquake.usgs.gov/fdsnws/event/1/). All derived time series and detection scripts are released under the Creative Commons Attribution 4.0 International License (CC-BY 4.0). A DOI-linked Zenodo repository accompanies this preprint.

Acknowledgments

The author gratefully acknowledges USGS for open seismic data. This research was conducted independently without institutional funding; any views expressed are solely those of the author.

keywords

earthquakes; statistical methods; time series analysis; early warning; metronomic field; crustal dynamics; temporal coherence; scalar field theory

References

[1] United States Geological Survey (USGS), 2024, USGS Earthquake Catalog (FDSN Event Web Service). Public domain data, https://earthquake.usgs.gov/fdsnws/event/1/.

[2] Allen R. M., Melgar D., 2022, Annual Review of Earth and Planetary Sciences, 50, 47–75. DOI: 10.1146/annurev-earth-031720-074355.

[3] Böse M., Heaton T., Hauksson E., et al., 2019, Geophysical Journal International, 216, 1–18. DOI: 10.1093/gji/ggy388.

[4] Cochran E. S., et al., 2020, Seismological Research Letters, 91, 1963–1975. DOI: 10.1785/0220190314.

[5] Hoshiba M., 2021, Earth, Planets and Space, 73, 100. DOI: 10.1186/s40623-021-01410-8.

[6] Hui L., Ostriker J. P., Tremaine S., Witten E., 2017, Physical Review D, 95, 043541. DOI: 10.1103/PhysRevD.95.043541.

[7] Jordan, T. H., 2019, Annual Review of Earth and Planetary Sciences, 47, 71–100. DOI: 10.1146/annurev-earth-053018-060346.

[8] Planck Collaboration, 2018, Astronomy & Astrophysics, 641, A6. DOI: 10.1051/0004-6361/201833910.

[9] Bekenstein J. D., 2004, Physical Review D, 70, 083509. DOI: 10.1103/PhysRevD.70.083509.

[10] Kadanoff L. P., 1963, Journal of Mathematical Physics, 4, 143. DOI: 10.1063/1.1703952.

[11] Penrose R., 2020, The Road to Reality (Revised Edition), Jonathan Cape, London.

[12] Danion, L. (2025). Metronomic Fields Q and P: Temporal Cadence and Memory in Gravitational Dynamics. Zenodo Preprint, https://doi.org/10.5281/zenodo.14750971. ORCID: 0009-0008-8733-8261.